Renewable Energy 208 (2023) 665–678

Contents lists available at ScienceDirect

Renewable Energy

journal homepage: www.elsevier.com/locate/renene

Temporal and spatial characterisation of tidal blade load variation for structural fatigue testing

Raymond Lam [a,1], Sergio Lopez Dubon [a,*,1], Brian Sellar [a,1], Christopher Vogel [b,1], Thomas Davey [a,1], Jeffrey Steynor [a,1]

[a] School of Engineering, Institute for Energy Systems, The University of Edinburgh, Edinburgh, EH9 3DW, UK
[b] Department of Engineering Science, University of Oxford, Oxford, OX1 3PJ, UK

ARTICLE INFO

Keywords:
Tidal turbine blades
Wave-induced loading
Centre of effort variation
Load fluctuation
Blade fatigue
Structural fatigue testing

ABSTRACT

To achieve the full potential of tidal stream energy, developers are incentivised to use larger blades on tidal turbines. This requires validation of blade structural designs through full-scale blade fatigue tests to de-risk the engineering process. However, the loading scenarios encountered in testing facilities and those in reality could be significantly different, which induces errors in blade loads and fatigue damage. Here we characterise the unsteady tidal blade load variation through model-scale experiment. It was found that the standard deviations of thrust load range between 200% and 637% of condition without waves. This results in an increase of predicted fatigue damage between 6% and 18%. It was observed that the centre of effort shifts towards the blade root when encountering wave crests of opposing waves, which has not been reported in the literature to date. To reduce errors in fatigue test while the centre of effort is fixed, matching blade shear forces should be sacrificed to match target bending moment at the root. Matching blade shear forces leads to a reduction of predicted fatigue damage ranges from 17% to 25%, which can induce errors in fatigue testing. We anticipate our findings would facilitate the development of fatigue testing of tidal turbine blades.

1. Introduction

Tidal stream energy has the potential to play a significant role in producing renewable electricity to meet the increasing energy demand and reduce emission pollution. To achieve that potential, developers are incentivised to design larger and more reliable tidal turbine blades, for producing more electricity in a cost-efficient manner. As such, structural validation of tidal blade designs becomes particularly important for accelerating commercial deployment of horizontal-axis tidal energy converters (TECs), which has led to the development of full-scale fatigue testing facilities such as FASTBLADE at the University of Edinburgh [1].

Most of the horizontal-axis TECs operate in harsh ocean environments and are subjected to complex and unsteady flow due to the interactions of shear, turbulence and wave-induced velocities [2]. These effects lead to temporal and spatial variation of loading across the rotor area of TECs. On the other hand, hydraulic actuators load blades at discrete locations along the blade span during fatigue tests. Thus, the loading scenarios encountered in testing facilities and those in reality could be significantly different. This, in turn, could lead to differences in blade fatigue damage. It is therefore important to understand the unsteady loading experienced by tidal blades and eliminate errors between testing and realistic loads, in order to accurately replicate ocean loading conditions in testing facilities.

There has been a significant amount of work reported in the literature regarding the assessment of blade loads and TEC performance under turbulence and waves through model-scale experiments and numerical simulations. Studies in [3–5] demonstrated that turbulent flow will lead to load fluctuations and cause fatigue in tidal turbine blades. The rotation of blades through a turbulent flow field would also lead to energy contributions at multiples of the turbine rotational frequency, often known as rotational sampling of turbulence [3,6]. Velocity shear also contributes to load fluctuations of TECs. Each blade encounters the shear profile every revolution and thus, it leads to load fluctuations at the rotational frequency of the turbine [7].

There are several key parameters that influence the unsteadiness of blade loads under wave–current conditions, including wave height, frequency, direction and hub height relative to the mean water level [8]. Yet, their underlying reasons for causing load fluctuations and increase in peak loads are mainly embodied in the variation of inflow velocity when the waves are propagating through the rotor plane, known as

* Corresponding author.
E-mail address: Sergio.LDubon@ed.ac.uk (S.L. Dubon).
[1] All the authors contributed equally to this paper.

https://doi.org/10.1016/j.renene.2023.03.117
Received 3 December 2021; Received in revised form 11 February 2023; Accepted 26 March 2023
Available online 28 March 2023

Nomenclature

$\bar{U}$	Mean current velocity (m/s)
η	Surface elevation (m)
λ	Tip speed ratio (–)
ρ	Fluid density (kg/m^3)
φ	Rotor angular position (deg)
$\hat{D}_{accumulated}$	Normalised fatigue damage (–)
A	Rotor area (m^2)
C_d	Drag coefficient (–)
C_p	Power coefficient (–)
C_t	Thrust coefficient (–)
CE	Centre of effort (m)
CE_r	Centre of effort ratio (–)
D	Rotor diameter (m)
$D_{accumulated}$	Accumulated fatigue damage (–)
$F_x(x)$	Flapwise load distribution (N)
F_{total}	Total forces on a blade (N)
f_{wave}	Observed wave frequency (Hz)
H	Target wave height (m)
P	Power (W)
Q	Torque (Nm)
R_x	Reaction force (N)
RBM_x	Flapwise root bending moment (Nm)
RPM	Rotational speed of rotor (RPM)
T	Thrust (N)
$T_{duration}$	Duration of the selected test period (s)
T_{total}	Total test period (s)
T_{wave}	Wave period (s)
T_{window}	Time window selected (s)
ADV	Acoustic Doppler Velocimeter
TEC	Tidal energy converter

wave–current interactions [9]. While waves have an impact on current, current direction also changes the physical form of waves. This leads to differences in the load response of a turbine blade subjected to opposing and following waves. Draycott et al. in [10] observed that following waves lead to greater load fluctuations than opposing waves at the same wave height and frequency, while Scarlett et al. in [11] reported that greater load fluctuations occur at higher wave frequencies for following waves than opposing waves, and highlighted that wave frequency has a larger influence on blade loads than wave height.

Wave action results in significant increase of peak turbine load, with peak thrust exceeding current-only values by 65% in opposing regular wave condition with measured wave height of 0.36 m, target wave frequency of 0.31 Hz and mean current speed of 0.81 m/s in a circular wave–current tank [10]. Another experimental study conducted in the same tank with a same mean current speed reported in [12] found that the standard deviation of thrust is 575% of current-only condition for opposing irregular waves with a significant wave height of 0.41 m and peak period of 2.37 s. Although standard deviations of loads with waves were more significant compared to that without waves (up to 40% of the mean values [13]), load mean values did not vary much as reported in [14–16], because they are dependent on the mean flow velocity. The variation of loading and performance of scaled TECs with respect to wave phase and water depth were shown in [17,18].

Although there have been a lot of studies on unsteady tidal flow and its influence on blade loads, their implications on full-scale blade fatigue tests and investigation of blade fatigue damage are insufficient. Yet, they are important to the development of TECs and tidal energy. Full-scale blade fatigue test facilities such as FASTBLADE allows conceptual blade designs to be tested and validated before deployment. This improves reliability and survivability of tidal turbine blades, thus, avoids expensive mistakes in the ocean and de-risks the engineering process. However, replicating ocean loading conditions in full-scale testing facilities is challenging. For instance, hydraulic actuators in FASTBLADE load blades at several discrete angled loading points along the blade span. Their positions are fixed throughout a fatigue test and their magnitudes of load provided is equal to each other. This results in a fixed centre of effort (CE) on the blade compared to a varying CE in reality. CE is a point on the blade where the application of total forces experienced by the blade would result in the same root bending moment produced by the distributed forces. The differences in load derived from fixed and varying CE can induce errors in blade fatigue tests.

Previous studies on CE in the tidal energy sector were conducted based on tower measurements. Model-scale experimental study in [12] found that there are large variations in the centre of effort of moments about the spanwise axis on the entire TEC structure (blades, body and tower), which indicates a considerable moment acts about the shaft. On the other hand, study in [19] discussed that centre of effort of moments about the spanwise axis is higher in the water column for opposing wave condition due to a higher wavenumber, and hence the overall force acts at a larger distance from the blade root. However, both studies did not include the investigation of the CE of a turbine blade, and neither did the authors discuss the implications of CE variations of a blade on structural fatigue testing and corresponding fatigue damage.

This article addresses this aspect by studying the CE of tidal turbine blades, which has been little explored to date. In this article, the CE variation of a 1:15 scale tidal turbine in the presence of shear, turbulence and regular waves is explored and reported through time domain, frequency domain and statistical analysis. The time-series pattern of CE variation is particularly analysed to understand its relationship with wave phase. In addition to exploring the CE variation, load fluctuations under varying unsteady flow conditions are analysed and compared for discussing its implications on blade fatigue. Furthermore, the implications of CE variation on eliminating errors between fatigue testing and realistic loads are discussed.

2. Experimental configuration and test methodology

2.1. FloWave facility

All the experimental work presented herein was carried out at the FloWave Ocean Energy Research Facility (FloWave), located at the University of Edinburgh in the UK [20]. FloWave is a circular test tank combining waves and current, with 168 wavemaker paddles surrounding the entire circumference and 28 impeller units installed below the test area to recirculate current through turning vanes and flow condition filters, as illustrated in Fig. 1.

The tank has a diameter of 25 m with a nominal water depth of 2 m. The buoyant raisable floor is located at the centre of the tank with a diameter of 15 m, representing the test area where model tidal turbines are placed and installed. The arrangement of impellers and turning vanes allows the generation of predominantly straight recirculating current flow especially at the centre of the tank. Meanwhile, the wavemakers also enable waves to be added to the current flow field at any relative angle. More information about the current flow and waves creation mechanism can be found in [22].

The test tank is capable of generating a maximum current velocity of 1.6 m/s. The wave frequency on the other hand, ranges from 0.2 to 1.2 Hz with a maximum wave height of 0.45 m at a frequency of 0.5 Hz [10]. At the central test zone where the model turbine in this study is located, the streamwise current profile varies with depth due to the shear effect. Furthermore, the streamwise velocity gradient increases with increased mean streamwise flow velocity due to increased

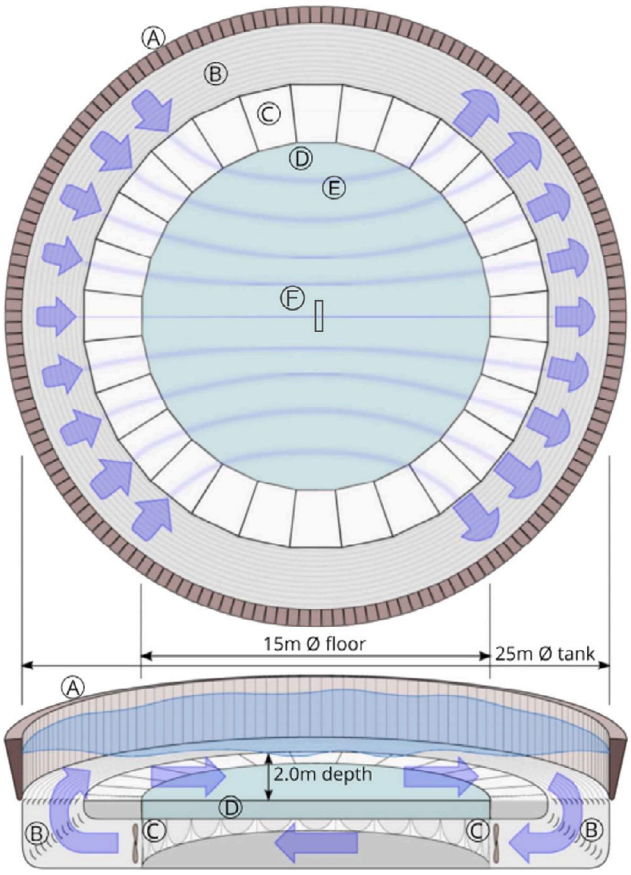

Fig. 1. Schematic of FloWave in plan and oblique section, illustrating: (A) wavemaker paddles, (B) turning vanes and flow condition filters, (C) current drive impellers, (D) buoyant raisable floor, (E) representation of the approximate path of the bulk current flow, and (F) turbine rotor position at the central test zone.
Source: Adapted from [21].

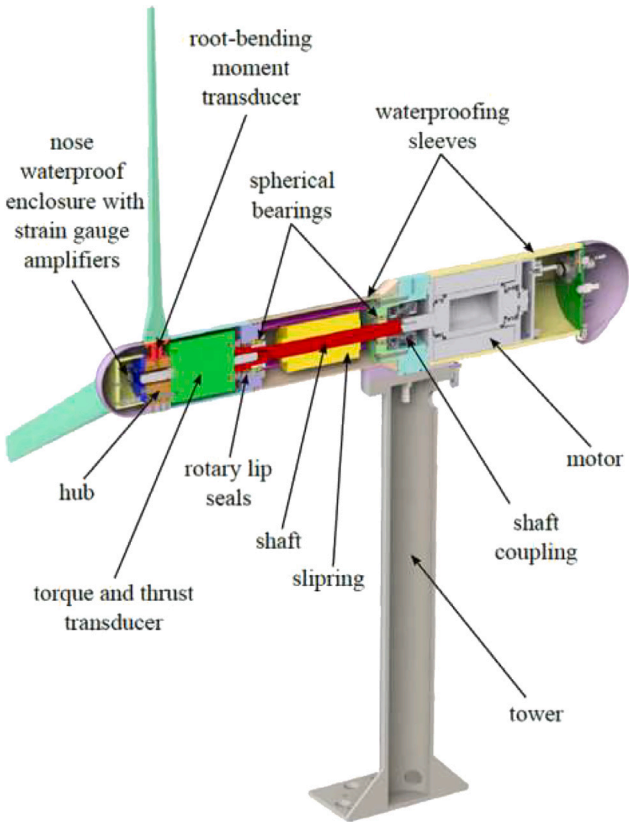

Fig. 2. Sectional view of the model turbine with main components annotated.
Source: Adapted from [24].

friction at the bottom boundary. Turbulence is also considered in the test tank. However, the arrangement of the tank does not allow control of turbulence intensity and it is approximately 7% at the hub height of model turbine used in this study. More details of the characterisation of current velocity and turbulence can be found in [21,23].

2.2. Model turbine

The horizontal-axis model turbine used in the experimental work is 1:15 scale, 3-bladed and bottom mounted. The rotor diameter (D) is 1.2 m with a hub height of 1 m from the bed. The hub diameter is 0.12 m and thus, the blade length from root to tip is 0.54 m. The model turbine is installed with transducers and a drive system to measure flapwise root bending moment of the blades (RBM_x) as well as rotational speed of the rotor (RPM), rotor angular position with respect to Z-axis (φ), thrust (T) and torque (Q) on the overall rotor. The RBM_x is also equivalent to the streamwise root bending moment. The drive system used is a brushless permanent magnet servo motor with direct drive design which is fitted with an encoder to record the angular position of the rotor. The thrust (C_t) and power coefficients (C_p) of the turbine as a function of tip speed ratio (λ) in a current-only condition can be found in [10]. A sectional view of the model turbine with main components is illustrated in Fig. 2. Detailed dimensions and design concepts of the model turbine is described in [24], while CAD files can be obtained from [25].

The model turbine has a target rotational speed of 70.7 RPM with motor speed control which corresponds to a nominal λ of 5.5. At the mean current velocity ($\bar{U}$) of 0.81 m/s, the chord based Reynolds numbers vary between 0.39×10^5 at the root and 1.96×10^5 at the tip. The rotor diameter based Reynolds number is 9.75×10^5 throughout this study, while the Froude number of the test facility is 0.18. Both numbers specified here are based on $\bar{U} = 0.81$ m/s and do not account for the wave induced velocity.

2.3. Instrumentation and configuration

Apart from the model turbine and the transducers incorporated into its nacelle as shown in Fig. 2, additional instrumentation including Acoustic Doppler Velocimeter (ADV), wave gauge and load cell were used throughout the experimental work to measure additional variables as described in Table 1. The resistance-type wave gauge measures the surface elevation, the ADV measures current velocity upstream of the turbine, and the load cell mounted at the foundation measures the total forces and moments on the overall structure. The test setup showing the relative locations is presented in Fig. 3. Note that RBM_x was measured for individual blades, while T and Q were measured for the overall rotor. Unless otherwise specified, the following study analyses RBM_x and flapwise CE of one blade which is at the top dead centre when φ is 0 deg.

2.4. Test plan and effective sea state

To investigate the load response and CE of tidal turbine blades under turbulence and waves, tests selected for this study include turbulent and shear flow with and without waves. Regular waves were used, instead of irregular waves, to study the fundamental response of load and CE of blades from a less complex wave–current velocity field. Therefore, it is useful to isolate the response to different key wave

Table 1
Types of instrumentation and measured variables with positions relative to the rotor plane centre.
Source: Adapted from [12].

Type	Measured variables	Sample rate	Relative location (m)		
		(Hz)	X	Y	Z
Model TST instrumentation	RBM_x, RPM, φ, Q, T	256	0	0	0
ADV	u, v, w	100	−2.40	0	0.60
Wave gauge	η	128	0	0	–
Load cell	$F_{LC.X}$, $F_{LC.Y}$, $F_{LC.Z}$ $M_{LC.X}$, $M_{LC.Y}$, $M_{LC.Z}$	256	0.49	0	−1.00

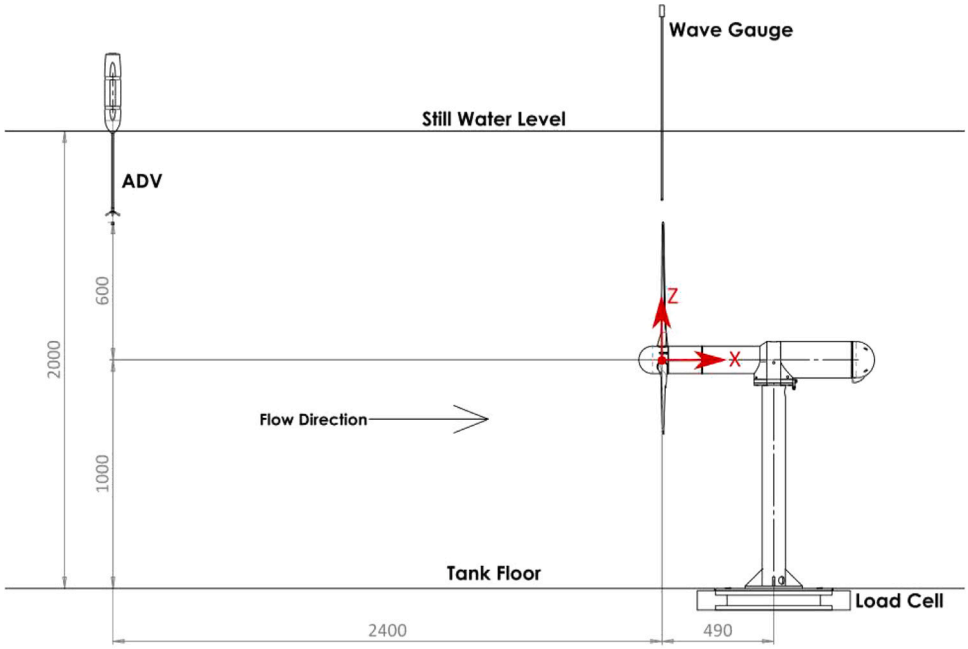

Fig. 3. Side view of the test setup illustrating the instrumentation relative to the centre of rotor plane (dimensions in mm) [12].

parameters. In this study, the test plan explores the effect of opposing and following waves, as well as wave height on the load response and CE of blades.

All the tests conducted in this study have $\bar{U}$ = 0.81 m/s with a streamwise turbulence intensity of approximately 7% at the rotor plane hub height of the model turbine. All the flow conditions also include the shear effect of the tank. More information about the measured shear profiles and turbulence intensity distributions at the rotor plane with the absence of the turbine can be found in [21]. The regular wave conditions have an observed (in the stationary reference frame of the facility) wave frequency (f_{wave}) of 0.4 Hz at the rotor plane with target wave height (H) of 0.1, 0.2 m for following waves and 0.1, 0.2, 0.4 m for opposing waves. To effectively compare the load response, a test condition of turbulence together with the velocity shear profile of the tank is included, making a total of 6 unsteady flow conditions. Note that the full-scale equivalents of target wave height and frequency can be obtained using Froude scaling [26]. The range of target wave height from 0.1 to 0.4 m in the tank corresponds to between 1.5 m and 6 m full-scale wave height while the target wave frequency of 0.4 Hz corresponds to 9.7 s full-scale wave period. This observed central frequency was a relatively commonly occurring condition in available observations from the tidal test site of the European Marine Energy Centre, Fall of Warness, Orkney, UK.

A constraint from the circular wave tank is that, the waves generated from the wavemaker paddles would reflect back at the opposite side which interferes with the incident waves at the rotor plane. Thus, constructive or destructive interference could be caused by the formation of partial standing waves. Fig. 4 illustrates an example of surface elevation (η) measured at the rotor plane with opposing waves at H = 0.2 m. Note that wave heights are reduced once reflected waves interfere with incident waves, and that wave heights are gradually increasing during the ramp up period. Therefore, stable waves which do not feature excessive deviations from the target wave conditions are selected specifically for time-series analysis, as annotated in Fig. 4. This ensures that the target wave heights are attained and that there are no interfering wave-induced velocities affecting the analysis of CE variation. Table 2 presents the target wave height, total test period (T_{total}), time window selected (T_{window}), and duration of the time window ($T_{duration}$) for each flow condition in this study. The $T_{duration}$ selected for all wave conditions is 7.5 s which corresponds to three complete wave cycles. There are approximately 9 rotor revolutions during this period. The T_{window} for time-series analysis of turbulence and shear condition was selected such that its $T_{duration}$ is the same as the conditions with waves.

However, all wave cycles except those in the ramp up region are used for statistical analysis of the wave conditions, while a period of 100 s within the T_{total} is used for turbulence and shear condition. This generally improves the quality of the statistical analysis by considering more load data, although the target wave heights in some of the wave cycles cannot be achieved. For spectral analysis, wave cycle selected for each wave condition is an integer such that there is no spectral leakage on the frequency components associated with wave-induced loads. The period selected for spectral analysis is the same for all unsteady flow conditions in this study (25 s with approximately 29 rotor revolutions). This ensures a fair comparison with the same frequency resolution.

Table 2
Unsteady flow conditions considered in the study with time selected for time-series analysis to ensure target wave height is achieved. Each regular wave condition has a target wave frequency of 0.4 Hz at the rotor plane.

Flow conditions	H (m)	T_{total} (s)	$T_{duration}$ (s)	T_{window} (s)
Following waves + turbulence + shear	0.1	40	7.5	11.55–19.05
Following waves + turbulence + shear	0.2	40	7.5	14.12–21.62
Opposing waves + turbulence + shear	0.1	70	7.5	25.97–33.47
Opposing waves + turbulence + shear	0.2	70	7.5	23.49–30.99
Opposing waves + turbulence + shear	0.4	70	7.5	20.92–28.42
Turbulence + shear		300	7.5	100.00–107.50

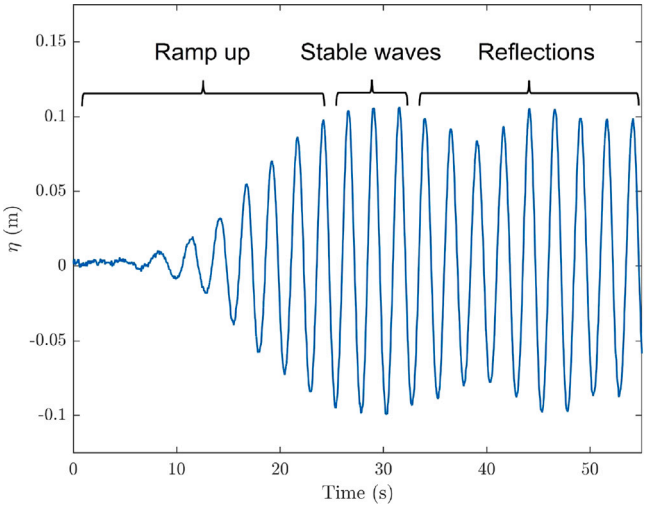

Fig. 4. Example of time-series surface elevation with opposing wave height of 0.2 m, illustrating regions of ramp up, stable waves and reflections — showing how the observed waves change in time across these three main temporal phases.

3. Centre of effort of a tidal turbine blade

Other than studying the load response of the blade and turbine mentioned in Table 1, this study also investigates the shifting of flapwise centre of effort (CE) along the blade span in the presence of axial loads under the aforementioned unsteady flow conditions. CE is a point along the blade span where the application of total forces experienced by a blade (F_{total}) at the same location would result in the same root bending moment as produced by the distributed forces over the span. The mathematical expression of CE is described in Eq. (1). It can be further scaled with the blade length (L) to produce the centre of effort ratio (CE_r) in Eq. (2). Note that F_{total} in Eq. (1) can be replaced by one-third of rotor averaged thrust ($T/3$) if only the flapwise direction is considered (Eq. (3)). In this study, the latter is used to evaluate flapwise CE_r because there are neither measurements of load distributions nor total forces on individual blades available. The drag force of the nacelle ($\frac{1}{2}C_d\rho\bar{U}^2A$) is estimated to be 1.81 N with a drag coefficient (C_d) of 0.5 being adopted, and is neglected in this study because its magnitude is insignificant compared to the measured rotor thrust.

$$CE = \frac{RBM}{F_{total}} \tag{1}$$

$$CE_r = \frac{CE}{L} \tag{2}$$

$$CE = \frac{RBM}{T/3} \tag{3}$$

Fig. 5 illustrates a schematic with flapwise load distributions of the blade under varying flow conditions that leads to increment or reduction of flapwise CE_r. The orange curve represents events which more lift (and drag) is produced (especially near the tip) such that load is distributed towards the tip region and thus, increasing the flapwise CE_r (as indicated by the position of orange arrow with arrow itself representing the total flapwise load acting on the blade). In contrast, the green curve demonstrates that lift (and drag) is curtailed due to events such as decreasing instantaneous axial flow velocity under the effect of waves. The reduction of lift near the tip region is more significant compared to that near the root. Therefore, the flapwise CE_r shifts to the root. Note that Fig. 5 only demonstrates loads in the flapwise direction. Edgewise loads are smaller than that in flapwise direction and were not instrumented.

4. Results

4.1. Time domain

4.1.1. Turbulence and shear

Fig. 6 presents the time-series flapwise root bending moment (RBM_x), thrust (T), power (P), blade angle (φ) and flapwise centre of effort ratio (CE_r) in the presence of turbulence and shear. The load data during the selected time window is split into three segments which are then time-shifted and synchronised to illustrate the repeatability of the load patterns. It is observed that the measured loads fluctuate in the presence of turbulence and shear, and do not demonstrate good repeatability as expected because of the randomness of turbulent flow. However, a trend is observed with higher flapwise CE_r at $\varphi = 0$ deg and lower flapwise CE_r at $\varphi = 180$ deg, which can be attributed to the effect of shear and tower shadow. This trend can also be seen in the spectral analysis presented in the later section.

4.1.2. Regular opposing waves with turbulence and shear

Fig. 7 presents the time-series load in the presence of regular opposing waves with target wave height of 0.1, 0.2 and 0.4 m under three consecutive wave cycles. The time-series pattern of the measured variables are time-shifted using η which is measured at a stationary position on top of the rotor plane. The x-axes of the plots are the time within a wave cycle which is scaled down by T_{wave}. It is apparent that there is a phase lag for φ between the consecutive wave cycles due to different phase relationships between the blade angle and wave phase. It is also evident that the fluctuations of RBM_x, T and P for all opposing wave conditions are dominated by the wave frequency. However, they have a negative correlation with η due to the opposing direction of waves propagation. This agrees with the results in [22] and can be attributed to the fact that the wave-induced velocity is reduced when the opposing wave crests are approaching the rotor plane. The same theory can be applied when the wave troughs are arriving at the rotor plane but the wave-induced velocity is increased, resulting in increased loading. Since the effect of waves is dominant on RBM_x of the blade as well as T and P of the turbine, it leads to reasonably good repeatability of responses for the three wave cycles.

Opposing waves also contribute to shape the time-series pattern of flapwise CE_r, as shown in Fig. 7. For $H = 0.2$ and 0.4 m, it is evident that there is a significant dip of flapwise CE_r at approximately $t/T_{wave} = 0.2$, immediately followed by an increase at $t/T_{wave} = 0.3$. At the second half of the wave cycle, less significant variations in flapwise CE_r are observed for $H = 0.4$ m. The time-series results show a good repeatability of the flapwise CE_r pattern for all wave cycles as presented, despite their slightly different phase relationship between the blade angle and wave phase. This, however, does not apply to the condition of $H = 0.1$ m, at which there is no evidence showing a strong correlation between the time-series pattern of η and flapwise CE_r.

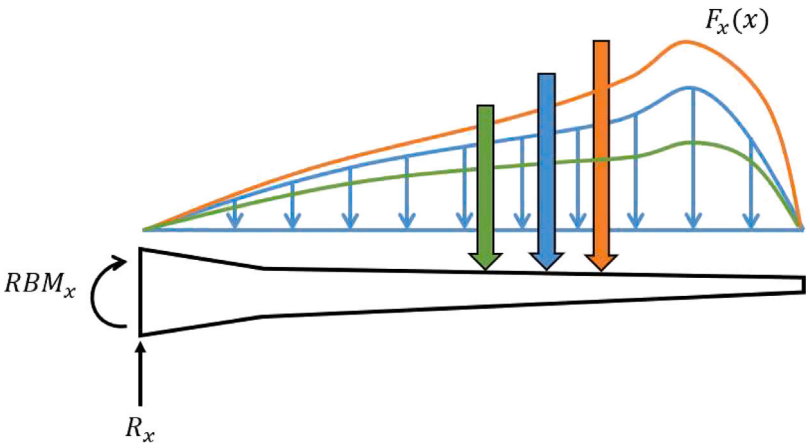

Fig. 5. Schematic demonstrating flapwise load distributions of the blade under different flow conditions with corresponding centre of effort and total axial force indicated by the positions of the arrows and arrows themselves.

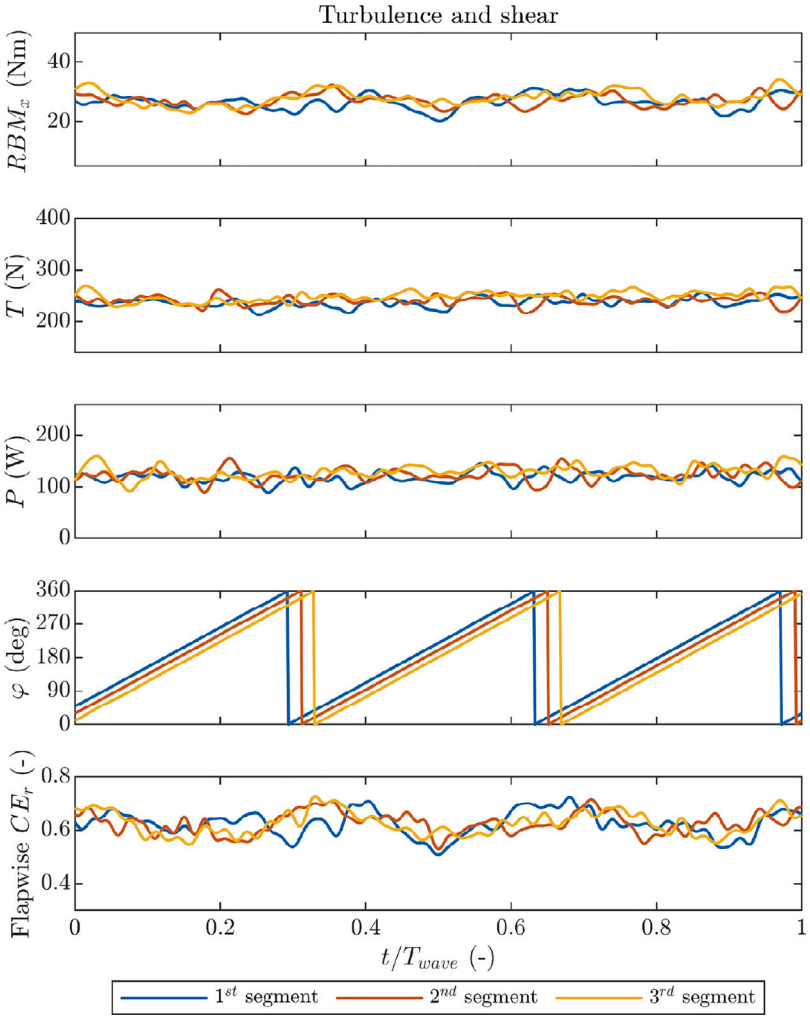

Fig. 6. Time-series blade data for turbulence and shear under three consecutive time segments within the selected T_{window}.

4.1.3. Time-series pattern of flapwise CE_r under regular opposing waves

To better investigate the cause of the flapwise CE_r pattern in the presence of opposing waves at $H = 0.2$ and 0.4 m, the flapwise CE_r from three consecutive opposing wave cycles are averaged and compared with surface elevation and blade angle, as shown in Fig. 8. It is observed that the flapwise CE_r for $H = 0.2$ and 0.4 m generally follows a similar pattern. At label A, the opposing wave crest is arriving at the rotor plane and thus, the wave-induced changes in velocity reduce the instantaneous axial flow velocity. At the same time, this results in a reduction in angle of attack of the blade and hence, less lift and drag is produced. Although the angle of attack decreases more at the blade root than near the tip, the reduction of lift near the tip region is more significant because the blade tip contributes a greater proportion of the total lift [27]. Therefore, there is a shift of flapwise

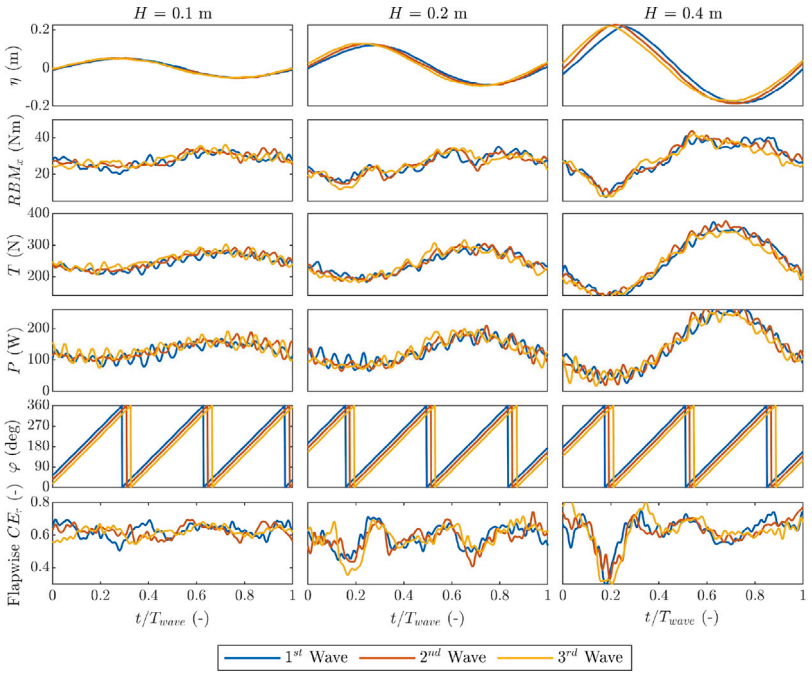

Fig. 7. Time-series blade data for regular opposing waves + turbulence + shear with H = 0.1, 0.2, 0.4 m and f_{wave} = 0.4 Hz (T_{wave} = 2.5 s) under three consecutive wave cycles.

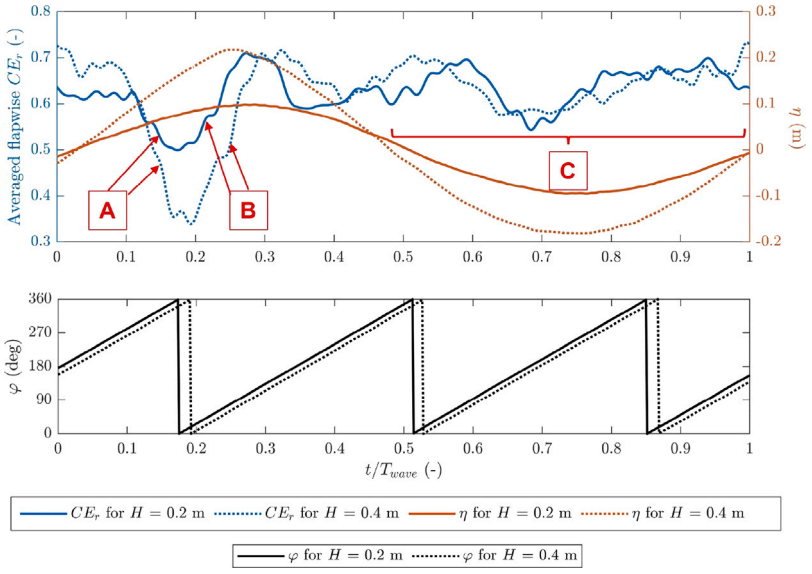

Fig. 8. Top: Averaged time-series flapwise CE_r from three consecutive opposing wave cycles for H = 0.2 and 0.4 m. Bottom: Time-series blade angle for H = 0.2 and 0.4 m. Solid lines represent H = 0.2 m while dotted lines represent H = 0.4 m.

Table 3
Corresponding key events for labels in Fig. 8.

Label	Event
A	Reduction of lift due to reducing instantaneous axial flow velocity
B	A sudden increase of flapwise CE_r as the opposing wave crest arrives
C	Variation of flapwise CE_r influenced by the blade rotational position

CE_r to the blade root at an approximate value of 0.35 for H = 0.4 m and 0.5 for H = 0.2 m, as reflected in the figure.

At label B, the flapwise CE_r is recovering from the local minimum and rising to approximately 0.7. This is not expected because the instantaneous axial flow velocity is minimum at the wave crest according to linear wave theory with wave–current interactions, whereas the flapwise CE_r starts to increase as the opposing wave crest arrives at the rotor plane. This phenomenon, however, is hard to fully explain because of the complex nature of fluid interaction in the vicinity of the rotor plane and difficulties in capturing the effect of attached and separated flow from the experimental setup. Meanwhile, the reduction of lift at A did not reduce the rotational speed of the turbine. In fact, the turbine rotational speed is seen to gradually vary throughout the wave period as illustrated in Fig. 9, although small fluctuations can be observed which can be attributed to the mass moment of the blade and tower shadow effect. Nevertheless, this shifting of flapwise CE_r towards the blade tip can be attributed to the increment of lift and drag near the tip due to increasing angle of attack.

In the second half of the wave cycle, labelled as C, less significant variations in flapwise CE_r are observed. The increase of flapwise CE_r can be attributed to the fact that the instantaneous axial flow velocity

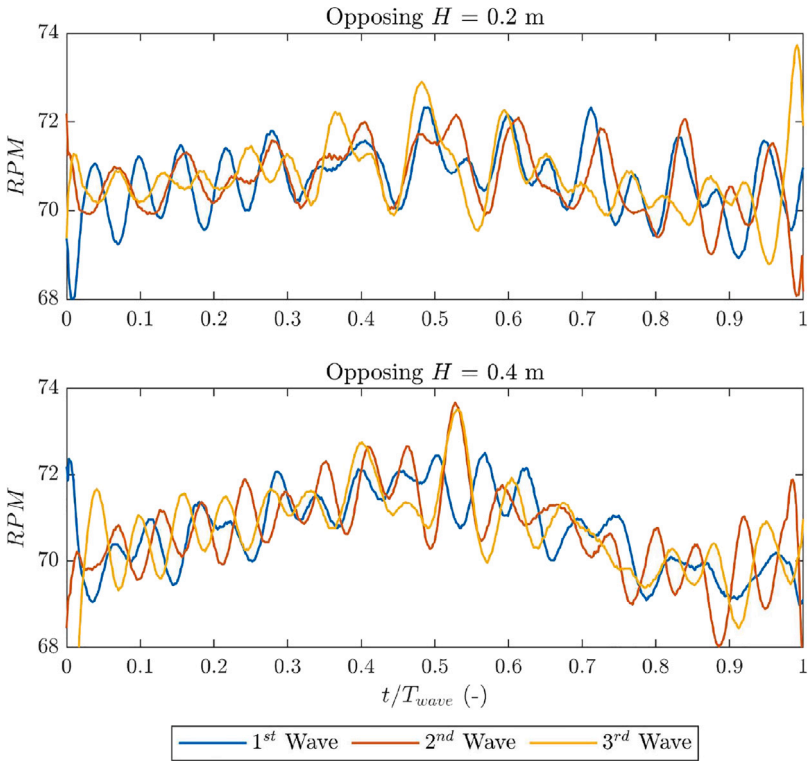

Fig. 9. Time-series RPM of the model turbine under at H = 0.2 and 0.4 m under three consecutive opposing wave cycles. Signal is smoothed to facilitate visualisation.

is increasing after the wave crest passes the rotor plane and the wave trough is arriving. Thus, the angle of attack increases and leads to increment of lift (and drag), especially near the tip region. This in turn results in loads distributed more towards the tip and hence, the flapwise CE_r increases to approximately 0.7. However, the flapwise CE_r drops to approximately 0.55 at t/T_{wave} = 0.7 afterwards. This is again unexpected because the instantaneous axial flow velocity should be increasing and thus, more lift (and drag) is produced near the blade tip which should in turn increase the flapwise CE_r. Instead, it is observed that the variation of flapwise CE_r in the second half of the wave cycle is influenced by the blade rotational position with a similar level of variation compared to that in turbulence with shear. A summary of key events with respect to the labels in Fig. 8 is presented in Table 3.

4.1.4. Regular following waves with turbulence and shear

Fig. 10 presents the time-series blade data and η in the presence of regular following waves with H = 0.1 and 0.2 m at a constant wave frequency, f_{wave} = 0.4 Hz (T_{wave} = 2.5 s) under three consecutive wave cycles. It is clear that the following waves at 0.4 Hz result in the same frequency of amplitude sweep for RBM_x, T and P. Unlike opposing waves, they have a positive correlation with η because the wave-induced velocity is maximum at wave crest and minimum at wave trough. However, the following waves do not have an apparent effect on the variation of flapwise CE_r. Nevertheless, the effect of shear and tower shadow is still observable which is reflected in a trend with higher flapwise CE_r at φ = 0 deg and lower flapwise CE_r at φ = 180 deg.

4.2. Frequency domain

Fig. 11 presents the amplitude spectra of RBM_x, T, P and flapwise CE_r at regular opposing and following waves in H = 0.1, 0.2 and 0.4 m with turbulence and shear. Amplitude spectra for turbulence and shear condition are also presented in the figure with the same scale to isolate the effect of waves. Large amplitude peaks at the f_{wave} are observed in RBM_x, T and P spectra in both opposing and following waves, with their amplitudes increasing with wave height. This is expected and agrees with the time-series results presented earlier in Section 4.1. Also noticeable in the RBM_x spectra is that the peak amplitudes at the target turbine rotational frequency, 1p, are fairly low compared to that at the f_{wave}. The rotational sampling of turbulence at multiples of 1p frequency is also negligible as observed in the RBM_x spectra. The same applies to the 3p amplitudes due to vertical shear and tower shadow in T and P spectra.

Side-band frequencies are observable in the RBM_x spectra at the turbine rotational frequency (1p) plus and minus the wave frequency (0.8 and 1.6 Hz). This can be attributed to the rotational sampling of waves reported in [12,28]. While the amplitude of this effect on the RBM_x spectra is comparable to the shear/tower shadow effect at 1p for opposing waves, it is fairly negligible for the following waves. This illustrates its dependency on the difference of wave-induced velocities across the rotor plane as well as the associated wavenumber. It is also evident that the amplitude peaks at the RBM_x spectra from rotational sampling of waves are negligible in T and P spectra. This is because the phase relationship between the rotating blades approximately cancelled out the associated rotor-averaged thrust [28].

For the amplitude spectra of flapwise CE_r, it demonstrates how much the CE shifts along the blade span and how frequent it shifts at this amplitude for the conditions in this study. It is clear that the amplitude peak of flapwise CE_r for turbulence and shear condition can be observed at 1p frequency, which agrees with the trend presented in the time-series analysis from 4.1.1. Besides, the amplitudes for all opposing wave heights at the wave frequency are lower than that at the side-bands and 1p frequencies. This is because the resulting change in CE at the wave frequency is cancelled out as the RBM_x and T are in phase. Moreover, the amplitudes of the side-band frequencies are higher than that of the 1p frequency for H = 0.4 m, while it is opposite for H = 0.1 and 0.2 m. This once again highlights the dependency of rotational sampling of waves on the difference of wave-induced velocities. Also noticeable in the flapwise CE_r spectra of wave conditions is the peaks at 2.0 and 2.4 Hz, corresponding to 2 times the

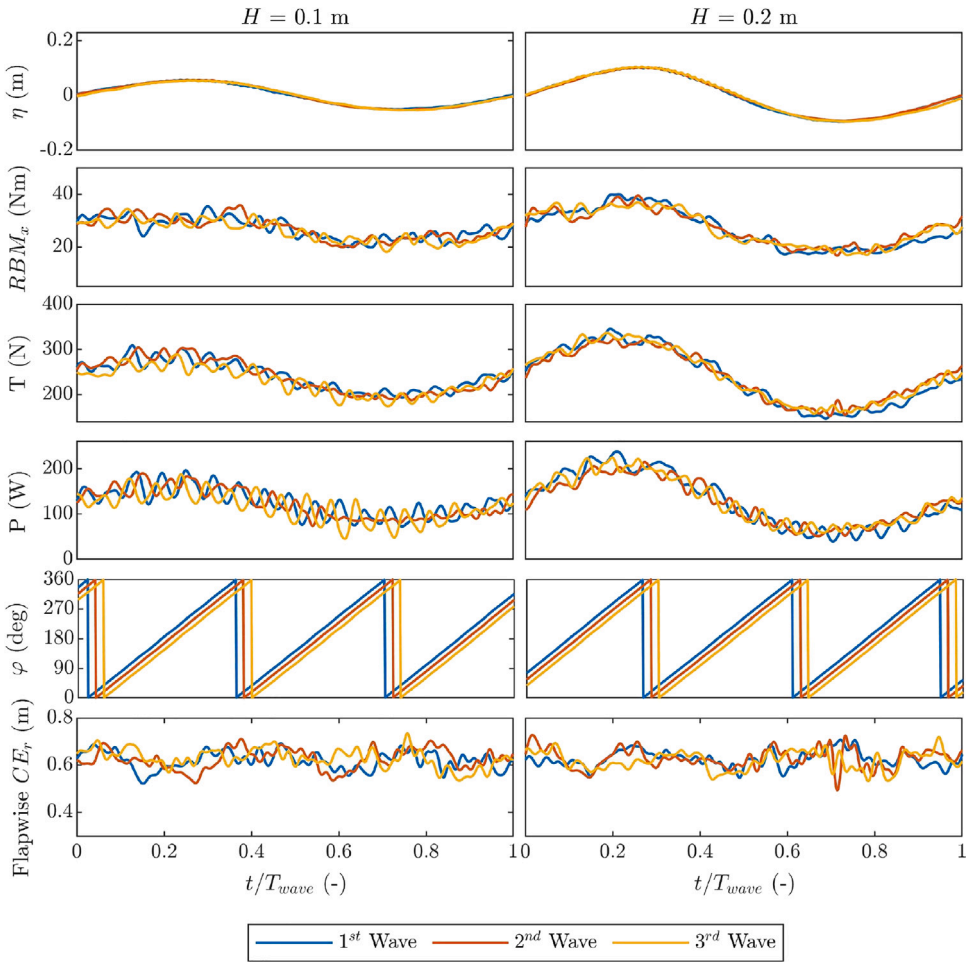

Fig. 10. Time-series blade data for regular following waves + turbulence + shear under 3 consecutive wave cycles with H = 0.1 and 0.2 m.

1p frequency minus the f_{wave} and 2 times the 1p frequency respectively. Although the effect that causes this is yet to be investigated, it is suspected that these two peaks are amplified as a result of dividing RBM_x by $T/3$ and local increase of RBM_x at those frequencies.

4.3. Statistical analysis of load fluctuation

To evaluate the results presented in Sections 4.1 and 4.2, statistical analysis of loads was conducted. Table 4 illustrates the means and standard deviations of key parameters of the model turbine with individual blades considered. It is apparent that the mean values of the measured loads and the flapwise CE_r do not alter significantly under different unsteady flow conditions, although their standard deviations are different. This is because the mean load values are dependent on the mean flow velocity rather than the unsteady flow conditions the blades experience. The mean values of RBM_x and flapwise CE_r on individual blades also shows reasonably good repeatability, implying that different phase relationship between blade angles and wave phase as well as the stochastic turbulent velocity fluctuations would not affect the mean values of individual blade loads. However, small discrepancies are observed for the standard deviations of individual blade loads which is likely due to the aforementioned different phase relationship between blade angle and wave phase.

Load fluctuations in the presence of waves are significantly larger than those without waves. When comparing the flow conditions with opposing waves to no-wave condition, the standard deviations of thrust load range between 200% and 637% of the equivalent value in no-wave condition as shown in Table 4. Meanwhile, the load fluctuations for following waves are greater than that for opposing waves when considering the same wave height, with standard deviations range between 126% and 162% of the opposing waves equivalents. This is expected because waves are elongated when in the same direction as the current, which results in a smaller wavenumber and reduces depth-attenuation of the wave-induced velocities. Likewise, the opposing waves shorten the wavelength and result in a higher wavenumber.

For the variation of flapwise CE_r, it is interesting to note that the standard deviations for opposing waves are larger than that for following waves equivalents, although the load fluctuations for following waves are more significant. Fig. 12 also captured such phenomenon with probability density function presenting the variations of flapwise CE_r for different unsteady flow conditions. It is evident that there is an increase in data spread comparing opposing waves to following waves. The same is true when the wave height increases from 0.1 to 0.4 m. This agrees well with the time-series results and amplitude spectra presented in Sections 4.1 and 4.2, from which the fluctuation of flapwise CE_r is more sensitive to opposing waves and higher wave heights. The significant dip of flapwise CE_r induced by opposing wave crests at every wave cycle can also be seen in the figure where there are more small extreme values for opposing waves at $H = 0.4$ m, essentially causing the data to be less well described by a normal distribution.

Another observation is that the standard deviation of flapwise CE_r in the presence of turbulence and shear is comparable to that with a combined effect of shear, turbulence and following waves at $H = 0.1$ m, although the load fluctuation in the presence of turbulence only is less. This can be attributed to the fact that more data in the turbulence and shear condition were selected for statistical analysis as well as the phase

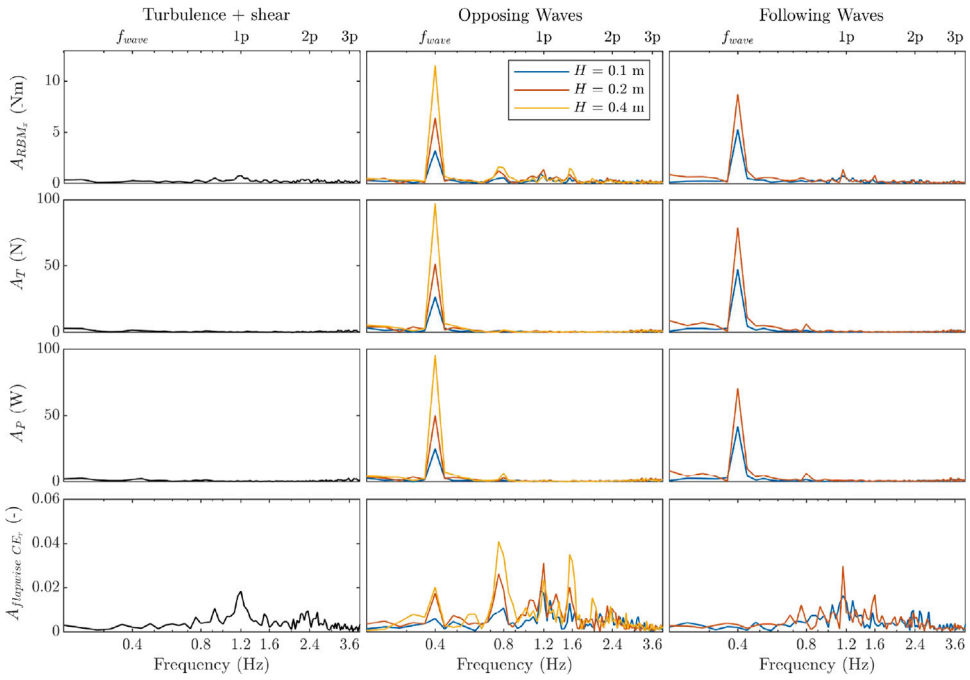

Fig. 11. Amplitude spectra of root bending moment, thrust, power and flapwise centre of effort ratio for no-wave condition with turbulence and shear, opposing and following regular waves with turbulence and shear. Multiples of the turbine rotational frequency: 1p, 2p and 3p are indicated on the top axis.

Table 4
Means and standard deviations of RBM_x, T, P and flapwise CE_r at regular following and opposing waves at H = 0.1, 0.2 and 0.4 m with turbulence (turbulence intensity of approximately 7%) and shear, as well as values at no-wave condition. Subscripts 0, 1 and 2 denote the individual blades of the model turbine.

	RBM_{x0} (Nm)	RBM_{x1} (Nm)	RBM_{x2} (Nm)	T (N)	P (W)	CE_{r0} (–)	CE_{r1} (–)	CE_{r2} (–)
Mean								
Turbulence + shear	27.5	27.5	27.5	245.7	126.7	0.623	0.623	0.623
Following (H = 0.1 m) + turbulence + shear	26.7	26.7	26.7	237.8	121.5	0.624	0.624	0.623
Following (H = 0.2 m) + turbulence + shear	27.6	27.6	27.6	245.8	132.3	0.625	0.625	0.623
Opposing (H = 0.1 m) + turbulence + shear	27.3	27.3	27.3	243.3	125.3	0.624	0.624	0.624
Opposing (H = 0.2 m) + turbulence + shear	26.9	26.9	26.9	239.3	124.0	0.623	0.623	0.622
Opposing (H = 0.4 m) + turbulence + shear	27.5	27.5	27.5	244.0	135.2	0.625	0.626	0.623
Standard deviation								
Turbulence + shear	2.17	2.16	2.22	10.9	12.8	0.0451	0.0460	0.0428
Following (H = 0.1 m) + turbulence + shear	4.15	4.16	4.33	35.4	33.3	0.0453	0.0457	0.0405
Following (H = 0.2 m) + turbulence + shear	6.70	6.66	6.85	59.0	54.2	0.0484	0.0494	0.0455
Opposing (H = 0.1 m) + turbulence + shear	3.22	3.12	3.23	21.9	23.7	0.0474	0.0480	0.0438
Opposing (H = 0.2 m) + turbulence + shear	5.23	5.27	5.46	38.7	39.0	0.0631	0.0633	0.0597
Opposing (H = 0.4 m) + turbulence + shear	8.72	8.63	8.83	69.4	69.8	0.0792	0.0795	0.0733

cancellation effect between RBM_x and T in following waves at H = 0.1 m.

5. Discussion

5.1. Implications of load fluctuation on blade fatigue

To compare the impact of unsteady loads and its associated load fluctuations on blade fatigue and peak loads, rainflow cycle counting method [29] was used to compress the experimental time-series RBM_x into a collection of local minimum and maximum, from which the equivalent load cycles are counted. The time window was selected to be 25 s with 10 wave cycles and approximately 29 blade revolutions. This is the same for all the unsteady flow conditions in this study and excludes the ramp-up period load data to ensure a fair comparison. Fig. 13 presents the histograms of RBM_x cycle range in the presence of various unsteady flow conditions selected for this study. It is evident that the load cycle range in the presence of turbulence and shear is less than that with regular waves, and that the load cycle range increases with wave heights which agrees well with the results demonstrated in Section 4.3.

To further quantify the fatigue damage from load fluctuations, Miner's rule [30] can be used to evaluate the accumulated damage as expressed in Eq. (4), where $D_{accumulated}$ is the accumulated fatigue damage, n_i is the number of cycles at stress level S_i and N_i is the number of cycles to failure at S_i. However, the blade structural performance of the model scale turbine is unknown and its corresponding $S-N$ curves are not available. To account for this, normalised damage, $\hat{D}_{accumulated}$ is used. The effect of cycle means is not presented in this analysis as it is deemed unnecessary. This is because the dominant mean load depends on the mean flow velocity. It is also observed that S is approximately linear and inversely proportional to N in other studies such as [31,32]. Therefore, $\hat{D}_{accumulated}$ can be expressed in Eq. (5) and is equivalent to the product of the load cycle range and its corresponding counts.

$$D_{accumulated} = \sum_{i=1}^{k} \frac{n_i S_i}{N_i S_i} \tag{4}$$

$$\hat{D}_{accumulated} = \sum_{i=1}^{k} n_i S_i \tag{5}$$

To evaluate the relative impact of load fluctuation due to the presence of waves, the $\hat{D}_{accumulated}$ under turbulence and shear provides

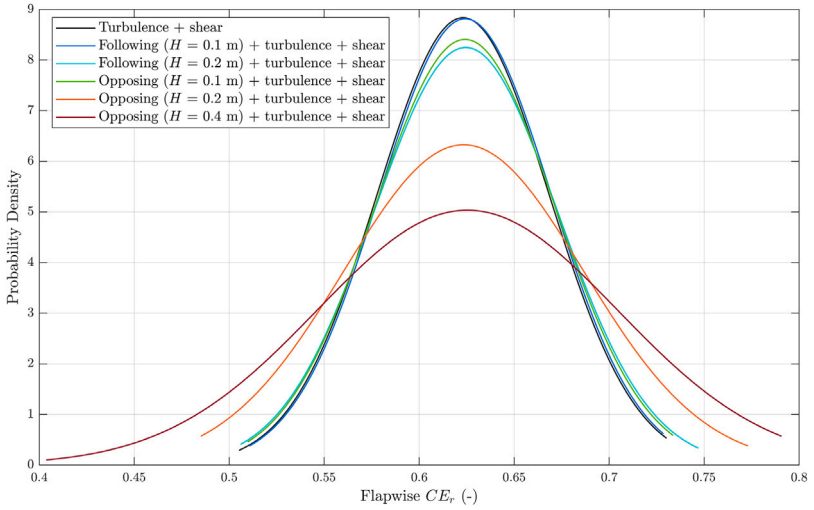

Fig. 12. Probability density function fitted with normal distribution (with a 99% confidence interval) for the variation of flapwise centre of effort ratio at different unsteady flow conditions.

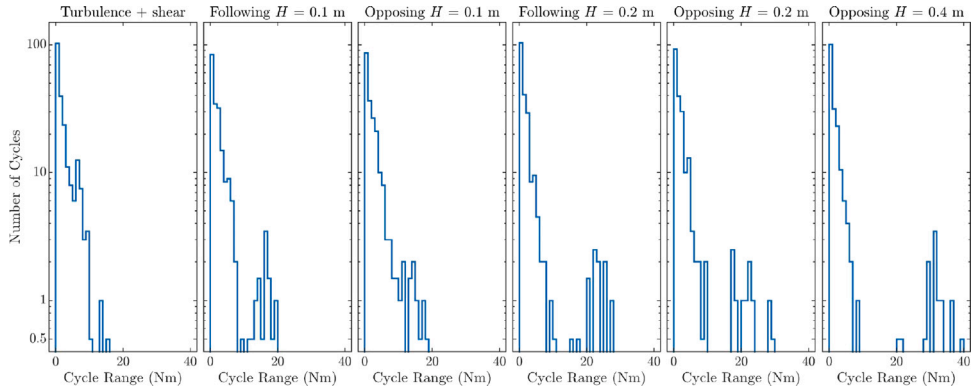

Fig. 13. Histograms of flapwise root bending moment cycle range in the presence of turbulence and shear, following and opposing regular waves at various wave heights. Half cycles are included in the number of cycles and cycle range bins are in 0.5 Nm increments.

Table 5
Percentage increase of normalised damage, $\hat{D}_{accumulated}$ and maximum RBM_x in waves conditions compared to no-wave condition.

	Following waves		Opposing waves		
	H = 0.1 m	H = 0.2 m	H = 0.1 m	H = 0.2 m	H = 0.4 m
$(\frac{\hat{D}_{accumulated,waves}}{\hat{D}_{accumulated,turbulence}} - 1) \times 100\%$	8.16%	11.0%	5.86%	12.2%	18.0%
$(\frac{\text{Maximum } RBM_{x,waves}}{\text{Maximum } RBM_{x,turbulence}} - 1) \times 100\%$	13.5%	31.3%	8.19%	26.6%	43.3%

the baseline case and is used to assess the increase in $\hat{D}_{accumulated}$ with waves. From Table 5, the increase in $\hat{D}_{accumulated}$ with waves ranges from 6% to 18% for the conditions selected in this study, which illustrates the need to consider wave-induced loadings into both fatigue analysis and blade fatigue tests. Moreover, the increase in maximum RBM_x in the presence of waves ranges from 8% to 43%, which is also shown in Table 5.

5.2. Implications of centre of effort variation on full-scale blade fatigue tests

From Fig. 12 in Section 4.3 it is clear that the variation of flapwise CE during unsteady flow is significant, with a maximum range of 37% of the blade length in opposing wave condition at H = 0.4 m. To efficiently fatigue test a full-scale tidal turbine blade, the positions of hydraulic actuators would be fixed during the fatigue test which results in a constant CE. However, the bending moment at the blade root during fatigue test would be different compared to that experienced by the blade in reality because the total axial forces of a blade acts at a fixed CE in the testing environment.

Fig. 14 illustrates the histograms of RBM_x cycle range derived from $T/3$ with a fixed flapwise CE_r of 0.623 taken from the average of the distributions, whereas Table 6 presents the comparison of $\hat{D}_{accumulated}$ and maximum RBM_x between that derived from $T/3$ and measured at the blade root. It is evident that the RBM_x cycle range derived from the thrust averaged from all blades has a smaller magnitude for all the unsteady flow conditions selected for this study when compared to Fig. 13. This leads to a reduction of fatigue damage ranges from 17% to 25% and peak RBM_x from 4% to 17%, which would induce errors in blade fatigue tests and thus implies that root bending moment should not be sacrificed for fixing the positions of hydraulic actuators. To overcome this, matching blade shear forces could be sacrificed to match the target bending moment at the root as the centre of effort is fixed throughout the fatigue test. Fig. 15 presents the measured thrust averaged from all blades with varying CE and the new averaged thrust

Table 6
Percentage ratio in normalised damage and maximum RBM_x derived from thrust averaged across all blades to that measured at the blade root.

	Turbulence	Following waves		Opposing waves		
		H = 0.1 m	H = 0.2 m	H = 0.1 m	H = 0.2 m	H = 0.4 m
$\frac{\hat{D}_{accumulated} \text{ from } T/3}{\hat{D}_{accumulated} \text{ from measured } RBM_x} \times 100\%$	82.6%	81.8%	78.7%	82.5%	81.0%	74.8%
$\frac{\text{Maximum } RBM_x \text{ from } T/3}{\text{Maximum measured } RBM_x} \times 100\%$	95.9%	91.0%	90.2%	91.6%	82.9%	86.1%

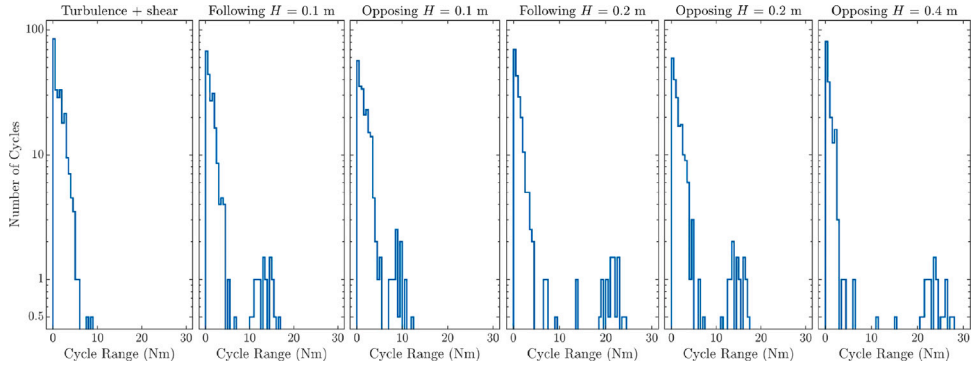

Fig. 14. Histograms of RBM_x cycle range derived from thrust averaged across all blades and fixed flapwise CE_r in various flow conditions. Half cycles are included in the number of cycles and cycle range bins are in 0.5 Nm increments.

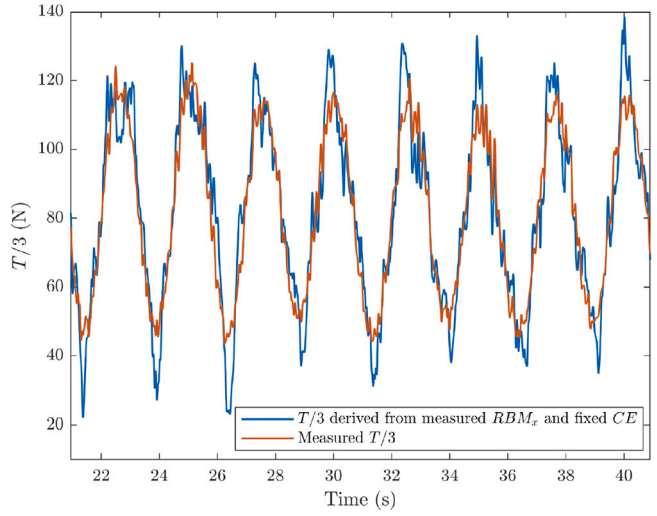

Fig. 15. Comparison of $T/3$ derived from measured RBM_x with a fixed flapwise CE_r of 0.623 and measured $T/3$ for opposing waves H = 0.4 m.

evaluated with fixed CE and measured RBM_x considering opposing waves at H = 0.4 m. To replicate the measured RBM_x with fixed positions of hydraulic actuators during the fatigue test, additional or reduced forces as indicated in the differences between the two curves, can be applied to the blade to recreate the bending moment at the root. Hence, the errors in fatigue damage for fixing the positions of hydraulic actuators could be eliminated.

Although the bending moment at the root recreated by this approach with fixed hydraulic actuators could be the same as the desired values, it should be noted that the actual bending moment distributions of the blade produced by the actuator loads could be different compared to that in real flow conditions. Hence, there will be benefits to acquiring more information about the bending moment distributions of the blade. Even though the accumulated damage considering blade root bending moment could be theoretically matched with the aforementioned approach, errors of bending moment at the root region between the mounting end and its nearest hydraulic actuator still exist. This inevitably would affect the analysis of blade fatigue life because this is the region where blades would fail due to fatigue [33]. The impact of such error on blade fatigue should be carefully evaluated. Nevertheless, the positions and angles of hydraulic actuators can be optimised to reduce the errors between actual and target bending moment distributions.

It is also recommended that developers should measure bending moment at the blade root and bending moment distributions as stated in IEC TS 62600-3:2020 [34], rather than rotor-averaged thrust only. This is indicated by the reduction of fatigue damage using RBM_x derived from thrust averaged across three blades and a fixed CE as discussed, as well as the amplitude reduction of thrust load. The cancellation effect of rotor thrust could exist due to the phase difference of individual blades. This reduces the amplitude of 3p thrust loading due to blade rotating through the shear layer which in turn, amplifies the flapwise CE_r. This amplification is undesirable because axial forces acting on individual blades do not experience such reduction of magnitude. As such, total forces on individual blades should be used to evaluate the CE if possible. This parameter is not available from experimental load data and thus, rotor-average thrust was used. However, it is reasonable to argue that the amplification effect of centre of effort is minimal in this study because the flow velocity field varies both temporally and spatially. Nevertheless, it demonstrates that more data regarding the load distributions and total forces of individual blade is required to eliminate the potential effect of artificial amplification of CE. Meanwhile, waves are irregular in nature although regular waves were used in this study to investigate the response of blade load and CE as well as to predict fatigue damage from a less complex wave–current velocity field. Further research will be conducted to study such responses and interactions in the presence of irregular wave conditions. The effect of varying wave frequencies on fluctuations of blade load and CE in the presence of regular wave conditions will also be explored, while the effect of phase relationship between waves and blade rotation on the variation of CE can be further investigated by conducting more tests to extract data within the period of stable waves.

It should be noted that there are more contributing factors for blade damage in real sea conditions other than cyclic loading, such

as extreme one-off loading [35], long-term composite degradation in seawater [36], erosion [37], etc. Such factors could be crucial in affecting the blade structural performance during real sea operations and would be useful to study along with fatigue loading.

6. Conclusions

Tidal turbine blades are subjected to complex and unsteady loading in harsh ocean environment which requires understanding of blade fatigue damage under such conditions. Potential error elimination approaches for differences between fatigue testing and realistic loads is important to efficiently validate the structural design of blades.

This paper focuses on evaluating the effect of shear, turbulence and regular waves on blade fatigue, load and centre of effort variation through experimental work. It was found that the maximum to mean root bending moment in the unsteady flow conditions selected for this study ranges between 124% and 184%. Additionally, standard deviations of thrust load in the presence of waves range between 200% and 637% of condition without waves. The effect of waves is prevalent in load fluctuations as peak load amplitudes were observed at the wave frequency. This results in an increase of predicted fatigue damage between 6% and 18% when compared to no-wave condition.

Centre of effort of the model-scale blade was found to be varying significantly in the presence of unsteady flow, with a maximum range of 37% of the blade length in opposing wave condition at the wave height of 0.4 m. A phenomenon that the centre of effort shifts towards the blade root at arriving wave crests in opposing waves was observed, which has not been reported previously in the literature. This was attributed to the reduction and increment of instantaneous axial flow velocity when the opposing wave crest is passing through the rotor plane. This in turn decreases and then increases lift generation near the blade tip region which causes the shifting of centre of effort.

To replicate bending moment at the root in unsteady flow conditions for fatigue testing full-scale blades while fixing the positions of hydraulic actuators, it was suggested that matching blade shear forces should be sacrificed to match the target bending moment at the root, as the former would lead to a reduction of predicted fatigue damage ranges from 17% to 25% for the conditions considered in this study. It is also recommended that developers should measure bending moment at the blade root and bending moment distributions as stated in IEC TS 62600-3:2020 in order to avoid errors in fatigue damage during blade fatigue testing.

Declaration of competing interest

The authors declare that they have no known competing financial interests or personal relationships that could have appeared to influence the work reported in this paper.

Acknowledgements

The authors are grateful for the financial support from the UK Engineering and Physical Sciences Research Council (EPSRC) through the SuperGen UK Centre for Marine Energy Research (EP/M014738/1) and project FloWTurb: Response of Tidal Energy Converters to Combined Tidal Flow Waves and Turbulence (EP/N021487/1). Support from the EPSRC, United Kingdom for funding the FloWave Ocean Energy Research facility (EP/I02932X/1) is also acknowledged. The second named author is supported by the European Union's Horizon 2020 research and innovation programme under the Marie SkÅodowska-Curie grant agreement No 801215 and the University of Edinburgh Data-Driven Innovation programme, United Kingdom. The authors are extremely grateful to all the staff at FloWave and others who worked on this series of experiments for their assistance in making this research possible.

References

[1] S.A. Lopez Dubon, C.R. Vogel, D. García Cava, F. Cuthill, E.D. McCarthy, C.M. Ó Bradaigh, Fastblade: A Technological Facility for Full-Scale Tidal Blade Fatigue Testing, 2023, pp. 1–22, http://dx.doi.org/10.2139/ssrn.4400928,

[2] T.A.A. Adcock, S. Draper, R.H.J. Willden, C.R. Vogel, The fluid mechanics of tidal stream energy conversion, Annu. Rev. Fluid Mech. 53 (1) (2021) 287–310, http://dx.doi.org/10.1146/annurev-fluid-010719-060207.

[3] I. Milne, R.N. Sharma, R. Flay, S. Bickerton, The role of onset turbulence on tidal turbine blade loads, in: 17th Australasian Fluid Mechanics Conference 2010, 2010, pp. 444–447, URL http://www.scopus.com/inward/record.url?scp=84856978625&partnerID=8YFLogxK.

[4] I.A. Milne, R.N. Sharma, R.G.J. Flay, S. Bickerton, Characteristics of the turbulence in the flow at a tidal stream power site, Phil. Trans. R. Soc. A 371 (1985) (2013) 20120196, http://dx.doi.org/10.1098/rsta.2012.0196.

[5] P. Ouro, T. Stoesser, Impact of environmental turbulence on the performance and loadings of a tidal stream turbine, Flow Turbul. Combust. 102 (3) (2019) 613–639, http://dx.doi.org/10.1007/s10494-018-9975-6.

[6] I.A. Milne, A.H. Day, R.N. Sharma, R.G.J. Flay, The characterisation of the hydrodynamic loads on tidal turbines due to turbulence, Renew. Sustain. Energy Rev. 56 (2016) 851–864, http://dx.doi.org/10.1016/j.rser.2015.11.095.

[7] K. Yahagi, K. Takagi, Moment loads acting on a blade of an ocean current turbine in shear flow, Ocean Eng. 172 (2019) 446–455, http://dx.doi.org/10.1016/j.oceaneng.2018.12.026.

[8] I.A. Milne, R.G.J. Flay, R.N. Sharma, S. Bickerton, The role of waves on tidal turbine unsteady blade loading, in: Proceedings of the 3rd International Conference on Ocean Energy, 2010, pp. 6–8, URL https://www.icoe-conference.com/publication/the_role_of_waves_on_tidal_turbine_unsteady_blade_loading/.

[9] N. Barltrop, K.S. Varyani, A. Grant, D. Clelland, X. Pham, Wave-current interactions in marine current turbines, Proc. Inst. Mech. Eng. Part M J. Eng. Maritime Environ. 220 (4) (2006) 195–203, http://dx.doi.org/10.1243/14750902jeme45, URL https://journals.sagepub.com/doi/abs/10.1243/14750902JEME45.

[10] S. Draycott, G. Payne, J. Steynor, A. Nambiar, B. Sellar, V. Venugopal, An experimental investigation into non-linear wave loading on horizontal axis tidal turbines, J. Fluids Struct. 84 (2019) 199–217, http://dx.doi.org/10.1016/j.jfluidstructs.2018.11.004.

[11] G. Thomas Scarlett, I.M. Viola, Unsteady hydrodynamics of tidal turbine blades, Renew. Energy 146 (2020) 843–855, http://dx.doi.org/10.1016/j.renene.2019.06.153.

[12] S. Draycott, J. Steynor, A. Nambiar, B. Sellar, V. Venugopal, Experimental assessment of tidal turbine loading from irregular waves over a tidal cycle, J. Ocean Eng. Mar. Energy 5 (2) (2019) 173–187, http://dx.doi.org/10.1007/s40722-019-00136-9.

[13] B.t. Gaurier, P. Davies, A. Deuff, G. Germain, Flume tank characterization of marine current turbine blade behaviour under current and wave loading, Renew. Energy 59 (2013) 1–12, http://dx.doi.org/10.1016/j.renene.2013.02.026.

[14] T.A. de Jesus Henriques, S.C. Tedds, A. Botsari, G. Najafian, T.S. Hedges, C.J. Sutcliffe, I. Owen, R.J. Poole, The effects of wave–current interaction on the performance of a model horizontal axis tidal turbine, Int. J. Mar. Energy 8 (2014) 17–35, http://dx.doi.org/10.1016/j.ijome.2014.10.002, URL https://www.sciencedirect.com/science/article/pii/S221416691400023X.

[15] P.W. Galloway, Performance quantification of tidal turbines subjected to dynamic loading (Ph.D. thesis), University of Southampton, 2013, URL https://eprints.soton.ac.uk/361524/.

[16] P.W. Galloway, L.E. Myers, A.S. Bahaj, Quantifying wave and yaw effects on a scale tidal stream turbine, Renew. Energy 63 (2014) 297–307, http://dx.doi.org/10.1016/j.renene.2013.09.030.

[17] E.E. Lust, L. Luznik, K.A. Flack, J.M. Walker, M.C. Van Benthem, The influence of surface gravity waves on marine current turbine performance, Int. J. Mar. Energy 3–4 (2013) 27–40, http://dx.doi.org/10.1016/j.ijome.2013.11.003.

[18] L. Luznik, K.A. Flack, E.E. Lust, K. Taylor, The effect of surface waves on the performance characteristics of a model tidal turbine, Renew. Energy 58 (2013) 108–114, http://dx.doi.org/10.1016/j.renene.2013.02.022.

[19] S. Draycott, J. Steynor, A. Nambiar, B. Sellar, V. Venugopal, Tidal Turbine Load Variability in Following and Opposing Irregular Wave Conditions, in: International Conference on Offshore Mechanics and Arctic Engineering, 9: Ocean Renewable Energy, 2020, http://dx.doi.org/10.1115/OMAE2020-18701, V009T09A004.

[20] D. Ingram, R. Wallace, A. Robinson, I. Bryden, The design and commissioning of the first, circular, combined current and wave test basin., in: Proceedings of Oceans 2014 MTS/IEEE Taipei, Taiwan, Institute of Electrical and Electronics Engineers (IEEE), 2014, pp. 1–7, http://dx.doi.org/10.1109/OCEANS-TAIPEI.2014.6964577, URL http://www.oceans14mtsieeetaipei.org/.

[21] D.R.J. Sutherland, D.R. Noble, J. Steynor, T. Davey, T. Bruce, Characterisation of current and turbulence in the FloWave ocean energy research facility, Ocean Eng. 139 (2017) 103–115, http://dx.doi.org/10.1016/j.oceaneng.2017.02.028.

[22] S. Draycott, D. Sutherland, J. Steynor, B. Sellar, V. Venugopal, Re-creating waves in large currents for tidal energy applications, Energies 10 (11) (2017) 1838, http://dx.doi.org/10.3390/en10111838, URL https://www.mdpi.com/1996-1073/10/11/1838.

[23] D.R. Noble, T.A.D. Davey, H.C.M. Smith, P. Kaklis, A. Robinson, T. Bruce, Spatial variation in currents generated in the FloWave ocean energy research facility, in: Proceedings of the 11th European Wave and Tidal Energy Conference (EWTEC2015), 2015, pp. 6–11.

[24] G.S. Payne, T. Stallard, R. Martinez, Design and manufacture of a bed supported tidal turbine model for blade and shaft load measurement in turbulent flow and waves, Renew. Energy 107 (2017) 312–326, http://dx.doi.org/10.1016/j.renene.2017.01.068, URL https://www.sciencedirect.com/science/article/pii/S0960148117300782.

[25] G.S. Payne, Experimental tidal turbine model external geometry CAD files and measurements data of tank tests carried out with that turbine model, 2017, http://dx.doi.org/10.7488/ds/1707.

[26] V. Heller, Scale effects in physical hydraulic engineering models, J. Hydraul. Res. 49 (3) (2011) 293–306, http://dx.doi.org/10.1080/00221686.2011.578914.

[27] F. Zilic de Arcos, C.R. Vogel, R.H. Willden, A parametric study on the hydrodynamics of tidal turbine blade deformation, J. Fluids Struct. 113 (2022) 103626, http://dx.doi.org/10.1016/j.jfluidstructs.2022.103626, URL https://www.sciencedirect.com/science/article/pii/S0889974622000755.

[28] S. Draycott, J. Steynor, A. Nambiar, B. Sellar, V. Venugopal, Rotational sampling of waves by tidal turbine blades, Renew. Energy 162 (2020) 2197–2209, http://dx.doi.org/10.1016/j.renene.2020.10.037.

[29] T. Endo, Damage evaluation of metals for random or varying loading, in: Proceedings of the 1974 Symposium on Mechanical Behavior of Materials, vol. 1, The Society of Material Science, Japan, 1974, pp. 371–380.

[30] T. Shimokawa, S. Tanaka, A statistical consideration of miner's rule, Int. J. Fatigue 2 (4) (1980) 165–170, http://dx.doi.org/10.1016/0142-1123(80)90044-4, URL https://www.sciencedirect.com/science/article/pii/0142112380900444.

[31] C.R. Kennedy, V. Jaksic, S.B. Leen, C.M. Brádaigh, Fatigue life of pitch- and stall-regulated composite tidal turbine blades, Renew. Energy 121 (2018) 688–699, http://dx.doi.org/10.1016/j.renene.2018.01.085, URL https://www.sciencedirect.com/science/article/pii/S0960148118300958.

[32] H. Sutherland, J. Mandell, Optimized goodman diagram for the analysis of fiberglass composites used in wind turbine blades, in: 43rd AIAA Aerospace Sciences Meeting and Exhibit, 2005, p. 196.

[33] P. Liu, B. Veitch, Design and optimization for strength and integrity of tidal turbine rotor blades, Energy 46 (1) (2012) 393–404, http://dx.doi.org/10.1016/j.energy.2012.08.011.

[34] BSI, Marine energy —Wave, tidal and other water current converters, IEC TS 62600–3:2020, BSI Standards Limited 2020, 2020, URL https://webstore.iec.ch/publication/60359.

[35] G.T. Scarlett, B. Sellar, T. Van Den Bremer, I.M. Viola, Unsteady hydrodynamics of a full-scale tidal turbine operating in large wave conditions, Renew. Energy 143 (2019) 199–213, http://dx.doi.org/10.1016/j.renene.2019.04.123.

[36] A. Boisseau, P. Davies, F. Thiebaud, Sea water ageing of composites for ocean energy conversion systems: Influence of glass fibre type on static behaviour, Appl. Compos. Mater. 19 (3–4) (2012) 459–473, http://dx.doi.org/10.1007/s10443-011-9219-6.

[37] L. Chernin, D.V. Val, Probabilistic prediction of cavitation on rotor blades of tidal stream turbines, Renew. Energy 113 (2017) 688–696, http://dx.doi.org/10.1016/j.renene.2017.06.037.